LOW POWER RECONFIGURABLE ANTENNA WITH CONTINUOUS BEAM STEERING CAPABILITY

by

Glendyn Darryn King

A thesis submitted in partial fulfillment
of the requirements for the degree

of

MASTER OF SCIENCE

in

Electrical Engineering

Approved:

Bedri A. Cetiner, Ph.D. Major Professor	Jacob Gunther, Ph.D. Committee Member
Reyhan Baktur, Ph.D. Committee Member	D. Richard Cutler, Ph.D. Interim Vice Provost of Graduate Studies

UTAH STATE UNIVERSITY
Logan, Utah

2021

ABSTRACT

Low Power Reconfigurable Antenna with Continuous Beam Steering Capability

by

Glendyn Darryn King, Master of Science

Utah State University, 2021

Major Professor: Bedri A. Cetiner, Ph.D.
Department: Electrical and Computer Engineering

The recent increase in the number of users and data consumption per user has created a need for larger bandwidth in electromagnetic communication. Higher frequencies allow for more bandwidth; however, higher frequencies present more propagation losses as compared to lower frequency bands. A way of meeting this bandwidth need is by utilizing phased array antennas (PAAs) with beam steering capabilities operating at higher electromagnetic frequencies. PAAs come with high cost and high power consumption. The designed reconfigurable antenna (RA) aims to tackle the issues of cost, power consumption, and loss. The designed RA achieves beam steering, therefore increasing the signal-to-noise ratio (SNR), using a new approach that results in low cost and low power consumption. This RA builds on previous designs with the novel approach of using varactor diodes. This varactor diode-based approach reduces the power consumption when compared with other methods such as PIN diode-based reconfigurable antennas while having the added benefit of being continuously steerable rather than having discrete steering directions.

(58 pages)

PUBLIC ABSTRACT

Low Power Reconfigurable Antenna with Continuous Beam Steering Capability

Glendyn Darryn King

Each year, the number of wireless devices increases, and the size of the devices' data is increases, 8k video streaming, for example. More and more bandwidth is needed for wireless networks to meet these growing demands. Higher frequencies allow for more bandwidth; however, using higher frequencies comes with some trade-offs. The higher the wireless signal frequency, the shorter the distance it can travel before the signal strength becomes too weak for the receiver to pick it up. One solution might be to increase the power of the signal provider, but that would waste a lot of energy. Most antennas radiate in all directions, so a lot of that extra power would be going up to space, or just away from the device it's trying to connect with, or it could be picked up as noise by a device on a different network. Instead, in many areas of research, including the research presented here, the issue is addressed by creating a better antenna. This research presents an antenna that focuses its radiated energy into a beam towards the target device. Focusing the power towards a device increases the signal's power going towards that device without much power going in undesired directions. If the target device moves, then the beam needs to be steered, so it keeps pointing at the device. The ability for an antenna to change something like the direction of its beam makes the antenna a reconfigurable antenna. Some reconfigurable antennas only have a few beam directions to choose from, so they would have to pick the closest one to the target device. The beam can be steered smoothly through any horizontal direction between two limits for this research. This research uses less power and fewer components to do so compared with some previous works.

This thesis is dedicated to my wife Sarah, whose dedication, sacrifices, and undying love and support has made it all possible.

I love you Sarah, thank you so much.

ACKNOWLEDGMENTS

I am grateful for my advisor Dr. Bedri A. Cetiner, who has been an amazing mentor throughout this entire endeavor, and without whom I would have been able to complete this project. I would also like to acknowledge the contributions and guidance of Dr. Md Asaduzzaman Towfiq, his insights at every stage of this process were invaluable.

Additionally, I am also very grateful to the members of my committee, Dr. Reyhan Baktur, and Dr. Jacob Gunther, for their help on this project and all the support and guidance through my undergraduate and graduate academic careers.

I would also like to thank the professors at Snow College for instilling an intense passion for learning, attention to detail, and starting me off on my academic journey.

Finally, I would like to thank my family, especially my parents, for their sacrifices that have allowed me to be where I am today.

Glendyn D. King

CONTENTS

Page

ABSTRACT iii

PUBLIC ABSTRACT iv

ACKNOWLEDGMENTS vi

LIST OF TABLES ix

LIST OF FIGURES x

ACRONYMS xii

1 INTRODUCTION 1

2 LITERATURE REVIEW 4
2.1 Phased Arrays 4
2.2 Reflectarrays 5
2.3 Transmitarrays 7
2.4 Intelligent Surfaces 8
2.5 PIN Diode Based MRA 8
2.6 MEMS Based MRA 10
2.6.1 Varactor Based MRA 10

3 RESEARCH AND DESIGN METHODS 12
3.1 Design Parameters 12
3.2 Antenna System Architecture 14
3.2.1 Feeding Layer 14
3.2.2 Antenna Layer 15
3.2.3 Parasitics Layer 15
3.3 Optimization Procedure 16
3.4 Design Methods and Project Objectives 16

4 MODELS 18
4.1 Varactor Model 18
4.2 Biasing Circuitry Model 20

5 WORKING MECHANISM FOR CONTINUOUS BEAM STEERING 23
5.1 Yagi Uda Model 23
5.1.1 Derivation of Analytical Model 24

6 FABRICATION 30
6.1 Fabrication Decisions 30
6.2 Fabricated Antenna 31
6.3 Non-functional Components 31
6.3.1 Anechoic Chamber 32
6.3.2 Mount 32
6.3.3 Power Supply 32

7 RESULTS 34
7.1 Characterization And Testing Of The Fabricated Antenna 34
7.1.1 Measurements 35
7.1.2 Reflection Coefficient Change with Varactor Bias Voltage 36
7.1.3 DC Power Consumption 36
7.2 Steering 37

8 CONCLUSION 43

REFERENCES 44

LIST OF TABLES

Table Page

3.1 Design parameter values 13

6.1 Bill of Materials 31

7.1 DC power consumed for various varactor reverse bias voltages 37

7.2 Measurements of half-power beam width, main lobe direction, and realized gain of the fabricated RA 39

7.3 Measurements of beam steering of the fabricated RA 39

LIST OF FIGURES

Figure		Page
1	Phased array antenna example using patch antenna elements in a planar array with 5 λ as an example dimension	5
2	Reflectarray with typical dimensions	6
3	Transmitarray with typical dimensions	7
4	Reconfigurable intelligent surface (RIS)	9
5	Monolithic multifunctional reconfigurable antenna system with typical dimensions	10
6	Exploded view of RA, the layers are shown separate to show detail, in reality the layers are bonded together.	12
7	Cross sectional view of antenna board	13
8	3D views of varactor based MRA board	14
9	Beam steering achived in full-wave analysis from optimized RA	17
10	Schematic of equivalent varactor circuit model	19
11	Varactor junction capacitance vs applied reverse bias voltage	20
12	Varactor series resistance vs applied reverse bias voltage	20
13	Parasitic Elements with Varactor Diodes and Chokes	22
14	Biasing circuit schematic diagram showing two varactor diodes along with four RF chokes	22
15	Basic Yagi-Uda diagram using dipole elements	24
16	RA structure consisting of the parasitic elements and driven patch element in space with θ and ϕ direction vectors shown	25
17	Placement of antenna elements in phased array model of RA system, 1 corresponds to the driven patch element, 2 and 3 correspond to the parasitic elements	26

18 Analytical field pattern solution compared with simulated full wave analysis for the $V_1 = 0.4\,\mathrm{V}$ and $V_2 = 18\,\mathrm{V}$ case 29

19 Analytical field pattern solution compared with simulated full wave analysis for the $V_1 = 18\,\mathrm{V}$ and $V_2 = 18\,\mathrm{V}$ case 29

20 Exploded 3D view of antenna board showing the milled cavity for housing the RF end launch connector 31

21 Photos of RA board 32

22 Reflection coefficent of fabricated RA compared with reflection coefficent of full-wave analysis simulation, both for the case of $V_1 = 0.4\,\mathrm{V}$, $V_2 = 18\,\mathrm{V}$ . . 35

23 Reflection coefficent of fabricated RA for three cases of applied bias voltages 36

24 Measured and simulated RA radiated patterns where $V_1 = 18\,\mathrm{V}$ and $V_1 = 18\,\mathrm{V}$ 40

25 Measured and simulated RA radiated patterns where $V_1 = 0.04\,\mathrm{V}$ and $V_1 = 18\,\mathrm{V}$ 40

26 Measured and simulated RA radiated patterns where $V_1 = 18\,\mathrm{V}$ and $V_1 = 0.04\,\mathrm{V}$ 41

27 Measured and simulated RA radiated patterns where $V_1 = 0.04\,\mathrm{V}$ and $V_1 = 10\,\mathrm{V}$ 41

28 Measured and simulated RA radiated patterns where $V_1 = 10\,\mathrm{V}$ and $V_1 = 0.04\,\mathrm{V}$ 42

ACRONYMS

ABS	Acrylonitrile Butadiene Styrene
EM	Electromagnetic
HFSS	High Frequency Simulation Software
MEMS	Micro-Eectro-Mechanical Switch
MRA	Multifunctional Reconfigurable Antenna
MRAA	Multifunctional Reconfigurable Antenna Array
PAA	Phased Array Antenna
PCB	Printed Circuit Board
PIN	Positive-Intrinsic-Negative
RA	Reconfigurable Antenna
RF	Radio Frequency
RIS	Reconfigurable intelligent surfaces
RLC	Resistor Inductor Capacitor
SMA	SubMiniature version A
SMP	SubMiniature Push-On
SNR	Signal to Noise Ratio
VNA	Vector Network Analyser

CHAPTER 1

INTRODUCTION

Increasing demand for larger, faster, more reliable data, along with an explosion of user growth and a need for low–power & high-efficiency systems, has created a need for innovation in many areas of wireless communications [1]. A straightforward way of increasing data rates is to increase the communications bandwidth. Scarcity of bandwidth at low frequencies has prompted the utilization of higher frequencies, most recently millimeter-wave bands, i.e., 20 – 80 GHz, where large swaths of frequency spectrum, i.e., bandwidth, are available. However, increases in electromagnetic (EM) propagation losses at higher frequencies make wireless communication challenging. Phased array antennas, where multiple antenna elements are used together with phase shifters, overcome this loss by increasing directivity and steering their beams towards a target user to maximize the signal-to-noise ratio (SNR). Phased array antennas come with a number of their own drawbacks, such as high power consumption, complexity, and high cost. Multifunctional reconfigurable antennas (MRAs) have recently gained popularity because they accomplish what the phased array approach would with far simpler system architecture and less power consumption by combining multiple functions into single antenna elements [2]. There have been a number of recent works in MRAs which show their viability in overcoming the challenges faced by phased arrays. [3, 4]

An MRA has the ability to dynamically change some number of its parameters such as polarization, radiation pattern, and beam direction. An MRA is advantageous due to the increased efficiency and transferred power resulting from steering its beam at an individual radiator level without a phase-shifting network. In a typical MRA architecture, above the driven antenna is the parasitic layer which contains an upper surface composed of a grid of electrically small metallic patches called pixels. [5] This upper surface is called the reconfigurable parasitic pixel surface. The reconfigurable parasitic pixel surface's reactive

loading is varied by connecting and disconnecting adjacent parasitic pixels by turning ON and OFF the interconnecting radio frequency (RF) switches. The reconfigurable modes of operation in frequency, polarization, beam-steering direction, and beam-width variability are achieved by proper reactive loading of the parasitic layer. This occurs due to the EM energy generated by the driven antenna that couples to the parasitic layer. In short, changing the geometry of the reconfigurable parasitic surface (i.e., changing the reactive loading) changes the RF current distribution on it, which in turn changes the antenna mode of operation in frequency, polarization, and radiation pattern. Depending on the change in reactive loading, antenna properties can dynamically be modified. For example, in the reconfigurable antenna (RA) for this research, the beam steering direction is changed while the polarization and frequency band of operation are kept fixed.

There are already several different approaches to making an antenna system reconfigurable. Each approach has strengths and weaknesses. Some of these approaches include PIN diodes, Micro-Electro-Mechanical Switches (MEMS), and varactor diode-based reflectarrays. These schemes have a similar underlying principle of changing the topology of a passive network of parasitic elements, which changes the overall radiated beam of the entire antenna system. The MRA schemes specifically rely on switching on/off parasitic elements placed in the near field of the driven antenna that achieve the desired behaviors. Challenges in the design of an MRA include trade-off considerations such as steering range, number of steering modes, system complexity, power use and efficiency, architecture size, and realized gain. Increasing the number of steering modes is desirable due to the increased number of center steering directions available. However, increasing the number of steering modes also increases power consumption, complexity, and size. This can be taken into account through the use of a varactor-based, continuously steerable beam due to the decrease in complexity and power consumption needed to achieve a similarly large number of steering modes when compared to methods relying on RF switches with two states (ON/OFF) such as PIN diodes. This research explores the viability of varactors to create a continuously steerable reconfigurable antenna (RA) rather than a RA with discrete steering modes.

The research problem addressed in this thesis is the design, simulation, and characterization of a RA with the capability of continuous beam steering. The approach to this problem is the utilization of varactor diodes as the switching elements in the RA. The antenna was designed and simulated by an EM full-wave analysis tool called ANSYS HFSS. The design of the RA for this research uses a patch antenna as its driven element operating in the Ka-band. The focus of the research was on the beam steering aspect. The antenna was characterized in an anechoic chamber using a vector network analyzer (VNA). The novelty of the research is to achieve continuous beam steering capability with low complexity and low power consumption with a varactor diode-based RA design. This research accomplishes three main objectives. The first objective is to design and simulate, with full-wave EM analysis, an RA with continuous beam steering capabilities using varactor diodes. The second and third objectives are the fabrication and characterization of the designed antenna. The success of this research is judged by the level of agreement between simulated and measured impedance and radiation pattern results.

CHAPTER 2

LITERATURE REVIEW

This chapter discusses previous research on antenna beam steering and beamforming approaches, along with current approaches being developed for 5G and 6G. Relevant aspects of these previous approaches are used to compare and contrast the work for this thesis to justify the motivation behind this research and show the novelty. The research approaches presented in this chapter include phased array antennas, reconfigurable intelligent surfaces, reflectarrays, transmitarrays, PIN diode-based MRAs, MEMS-based MRAs, and varactor-based MRAs.

The approaches presented in this chapter have a similar working mechanism in creating a signal phase gradient that causes beam steering. For the case of the phased array antennas, this phase gradient is from an external phase shifting network consisting of as many phase shifter components as the number of array antenna elements, which enables feeding each antenna element with the proper phase value to achieve a targeted phased gradient over the array. Reconfigurable intelligent surfaces (RIS), reflectarray, transmitarray, and the proposed varactor-based RA use a phase-shifting surface where the phases of the surface elements are controlled by controlling the EM coupling between the elements. This mechanism is contrasted against the phased array antennas as these approaches introduce the phase gradient after the EM wave is radiated.

2.1 Phased Arrays

A phased array antenna (PAA) is a system of two or more driven antenna elements and phase shifters. The phase shifters delay the feeding signal to each driven antenna element, which causes the total radiation pattern to steer. Phased arrays steer their beams faster and more efficiently than mechanically steering an antenna using motors. One area where phased array antennas play a significant role is radar. Early phased array radar systems

existed during World War 2, and PAAs are still used in radar systems to this day [6]. PAAs provide high gain, high directivity, and beamforming and steering; however, PAAs come at the cost of high power usage, complex controlling circuitry, and large overall size. A diagram of an example planar PAA system is shown in Figure 1 using side-fed patch antenna elements.

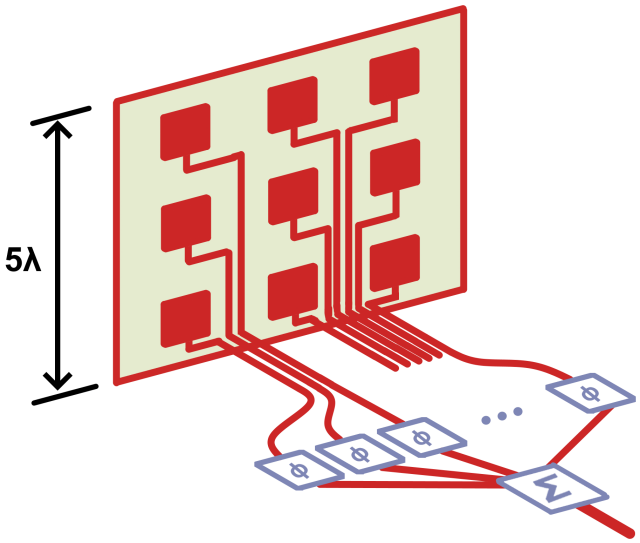

Fig. 1: Phased array antenna example using patch antenna elements in a planar array with 5 λ as an example dimension

2.2 Reflectarrays

Reflectarrays are an antenna system topology consisting of a reflecting surface and a primary radiator that illuminates the reflecting surface. The primary radiator is a feeding antenna, and the reflecting surface is a flat or curved surface with spaced elements that interact with the radiated field of the primary feeding radiator. Figure 2 shows a diagram of a reflectarray antenna system.

Reflectarrays combine some of the advantages of both aperture antennas and phased arrays. Reflectarrays possess the versatility of a phased array with the ability to produce multiple radiation patterns without the complex feeding system needed in a phased an-

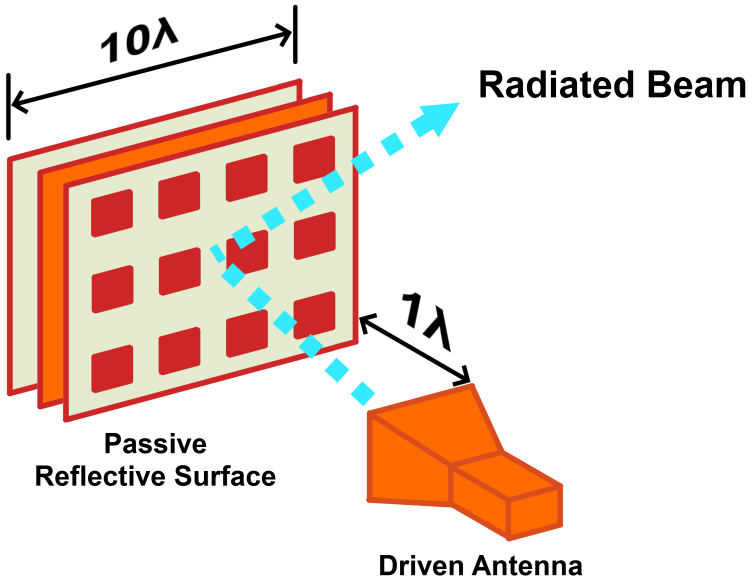

Fig. 2: Reflectarray with typical dimensions

tenna array [7]. Reflectarrays can be made steerable by mechanically altering the elements, such as mechanically rotating reflectors. These structures suffer from bulky sizes and large mounting platforms [8]. Reflectarrays can also be made steerable by electrically changing the impedance distribution of the reflecting surface with switching PIN diodes [9, 10], varactor diodes [11–14], MEMS [10, 11], etc, which mitigates the size challenges of mechanical reflectors.

While reflectarrays are smaller and less complex than phased arrays, reflectarrays have the added complexity of having the primary feeding radiator separate from the reflecting surface. A major consideration in the design of a reflectarray is the placement of the primary radiator. One aspect in the placement of the primary radiator is the distance between the primary radiator and the reflecting surface. If the primary radiator is too close to the reflecting surface, it causes illumination loss, where portions of the reflecting surface are unilluminated. The placement of the primary radiator should be such that the half-power beamwidth (HPBW) of the primary radiator's radiation pattern is the same as the subtend angle from the feed to the edges of the reflecting surface [15, 16].

The distance from the reflecting surface and the primary radiator is called the focal

distance. Major dimensions of a reflectarray can be on the order of 10λ, placing the focal distance of the primary radiator on the order of 1-10λ. Therefore the primary radiator is relatively far from the reflecting surface, which makes the overall system large. Another consideration in the placement of the primary radiator is its offset to avoid blocking loss, which is produced from the feeding antenna being in front of the reflecting surface.

2.3 Transmitarrays

The transmitarray, or array lens, is another antenna topology that, like the reflectarray, uses a primary radiator feeding antenna and a surface of elements that interact with the radiated fields from the feeding antenna. In the case of the transmitarray, the primary radiator illuminates one side of the array, and the radiation is produced on the opposite side [10]. Figure 3 shows a diagram of a transmitarray antenna system. This behavior of transmitarrays has the advantage over reflectarrays in that transmitarrays are free from feed blockage effects [10, 17].

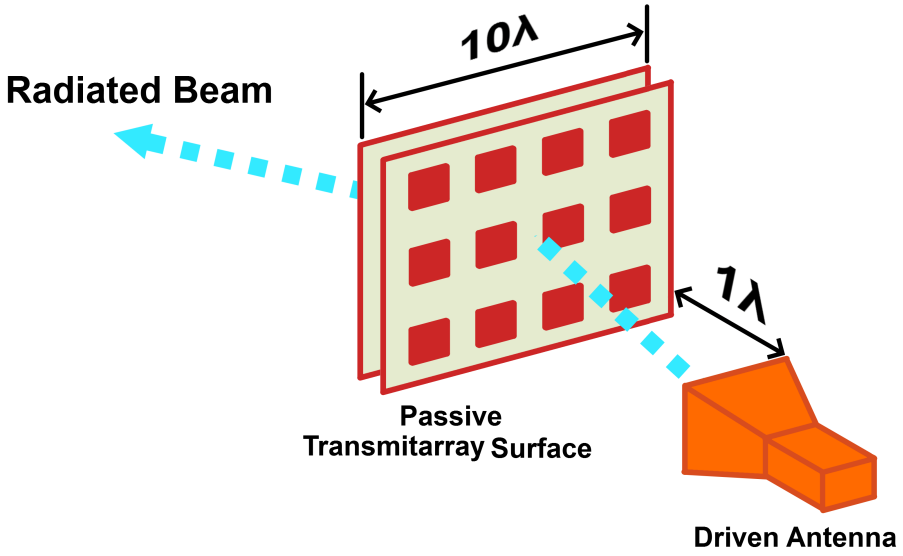

Fig. 3: Transmitarray with typical dimensions

A disadvantage of the transmitarray, when compared with the reflectarray, is that the design of a reflectarray is more straightforward than the design of a transmitarray

antenna because the reflectarray only needs to provide phase compensation for the incident wave, where the transmitarray must provide both the transmission and phase compensation simultaneously [17]. Like reflectarrays, the overall size of the transmitarray system is large due to the primary radiator being separate from the passive reconfigurable lens surface. These bulky sizes make reflectarrays and transmitarrays unsuitable for small devices such as cell phones.

2.4 Intelligent Surfaces

Reconfigurable intelligent surfaces (RIS), or hypersurfaces, are another approach to reduce EM propagation losses by controlling metamaterials embedded in any surface in the environment with software [18]. Intelligent surfaces are a software-controlled network of passive elements embedded into a planar surface in an environment such as an entire wall in a building, door, furniture, etc. Intelligent surfaces are comprised of dynamic metasurfaces. The metasurfaces are interconnected with phase switching elements. The macroscopic EM interaction of the metasurfaces is defined by the state of the switches [19].

Intelligent surfaces are an area of research that combines aspects of reflectarrays and transmitarrays in changing properties of a surface to reflect an incident EM wave at the desired angle or refract an incident EM wave at the desired angle. A major defining characteristic of intelligent surfaces is their size. Intelligent surfaces are extremely large compared with the wavelength of their operating frequency, on the order of 100λ. In addition to the large size of the intelligent surface itself, the radiating element is far from the intelligent surface. The radiating element can be placed inside the building structure that the RIS is built into or outside, such as a base station tower. Figure 4 shows a diagram of a RIS reflecting the signal from a base station to an end-user.

2.5 PIN Diode Based MRA

A beam-steering technique using PIN diodes changes parasitic elements' effective length and shape by electrically connecting or disconnecting segments together [4, 20–23]. The nature of PIN diodes and their binary states (ON/OFF) create discrete configurations.

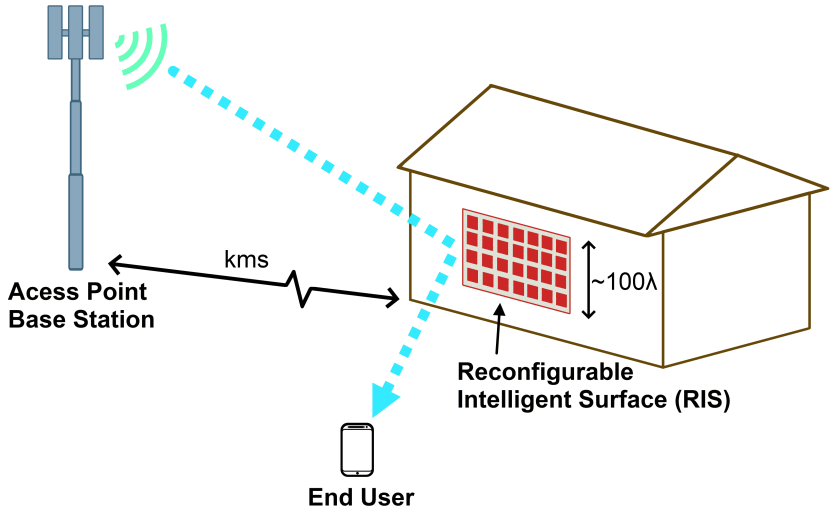

Fig. 4: Reconfigurable intelligent surface (RIS)

The maximum number of configurations is 2^n, where n is the number of PIN diodes. Some subset of these configurations will give a desirable antenna pattern with a tilted beam at the designed frequency and polarization. Elements of this subset are called modes. A large number of modes is desirable because each mode provides a desirable set of antenna parameters for a certain situation, and the more modes there are, the more versatile and robust the antenna is.

Accomplishing a low complex MRA design capable of generating many modes is key and is the main objective of this work. Varactor diodes can change the effective length by changing the electric length of a line with capacitive loading. The capacitance of the varactor diode changes continuously with the applied reverse bias voltage, leading to a continuously changing electric length. The continuous range of varactor diode states gives essentially infinite modes, reducing the number of needed components for some large number of needed modes from n to, e.g., 2. Another benefit that varactor diode-based RAs have over PIN diode-based RAs is the lower power consumption. There are fewer components than in the PIN diode design in [4], and varactors operate in reverse bias, which has significantly less current draw than in forward bias, as is the case for PIN diodes.

2.6 MEMS Based MRA

A similar technique to connecting and disconnecting parasitic elements with PIN diodes is connecting and disconnecting elements mechanically with MEMS technology [24–27]. The underlying principle remains the same as the PIN diode approach, specifically the use of a switch to connect/disconnect elements resulting in a configuration that changes the antenna's functionality. In the case of MEMS, the switch is mechanical rather than electrical, as with PIN diodes. MEMS switch-based MRAs have the advantage of monolithic integration with switching elements. However, the long-term reliability of MEMS switches remains a drawback. Figure 5 shows a diagram of an MRA system.

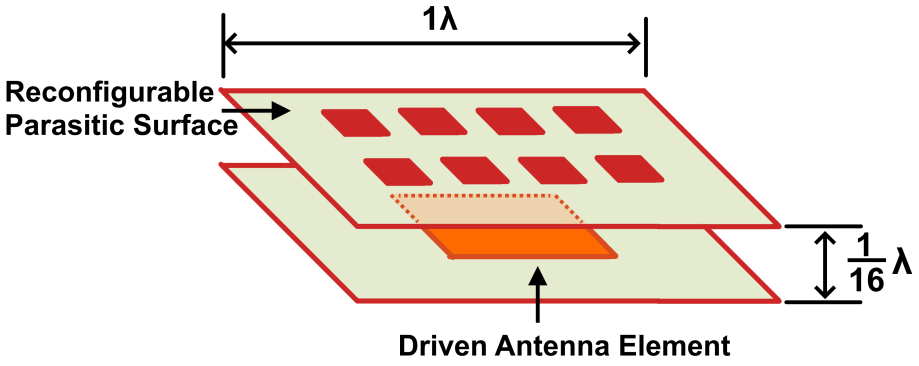

Fig. 5: Monolithic multifunctional reconfigurable antenna system with typical dimensions

2.6.1 Varactor Based MRA

Varactor diodes used in antenna design have included resonant frequency tuning using varactor connected stubs [28]. Beamforming by a loaded slot in the ground plane was also demonstrated [8]. Many other designs have been studied, with various steering techniques [28–30].

The design of a reconfigurable MRA rather than a reflectarray or transmitarray has many advantages, including reducing complexity from having a single monolithic system

rather than having a radiator and the reflectarray as separate systems. Another benefit is the broader bandwidth [17]. Reflectarrays and transmitarrays are primarily used on the basestation side due to their large sizes. An MRA could be used in either the basestation side, or the user side.

CHAPTER 3

RESEARCH AND DESIGN METHODS

In this chapter, the design of the antenna is discussed, including an outline of the design parameters and degrees of freedom which were adjusted to optimize the RA system based on key design objectives. This chapter also gives an overview of the multilayer printed circuit board (PCB) antenna architecture by presenting each layer with a description of its function. Finally, this chapter gives the design objectives met by this research. These design objectives acted as goals for each stage of the design process.

3.1 Design Parameters

The complete antenna system architecture is shown in Figure 6. A cross-sectional view of the side of the RA system is shown in Figure 7, with the PCB layers are stacked together.

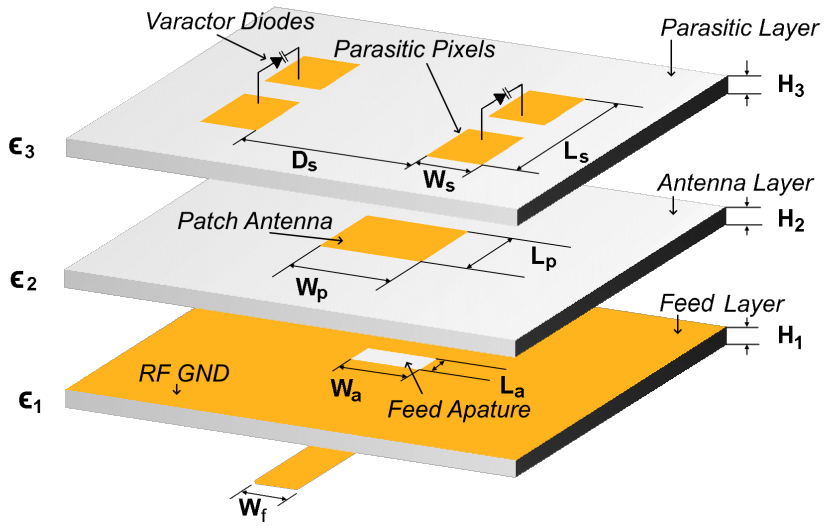

Fig. 6: Exploded view of RA, the layers are shown separate to show detail, in reality the layers are bonded together.

The degrees of freedom for the design are layer heights (H_1, H_2, H_3), antenna element's length (L_p) and width (W_p), the dielectric permittivity of each layer ($\epsilon_1, \epsilon_2, \epsilon_3$), feeding scheme for the patch antenna, which is an aperture coupled microstrip, and the parasitic pixel's size (L_s, W_s), shape, spacing (D_s). An electromagnetic full-wave analysis tool was used to optimize these design parameters. The final values for the design parameters are listed in Table 3.1.

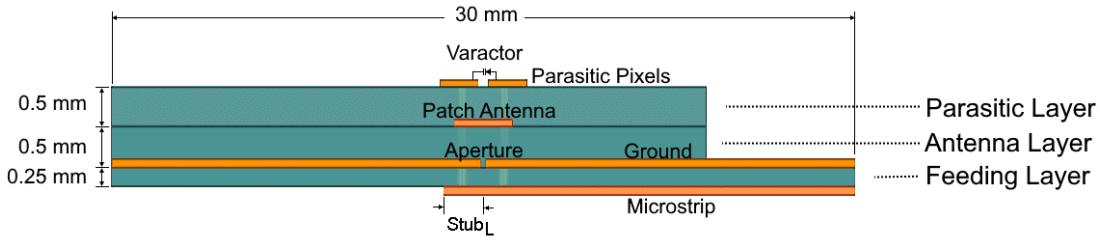

Fig. 7: Cross sectional view of antenna board

Table 3.1: Design parameter values

Parameter	Variable	Value	Unit
Feedline width	W_f	0.62	mm
Tuning stub length	Stub_L	1.5	mm
Aperture Width	W_a	2.4	mm
Aperture Length	L_a	0.205	mm
Patch Width	W_p	2.284	mm
Patch Length	L_p	2.284	mm
Parasitic Width	W_s	0.5	mm
Parasitic Length	L_s	3.5	mm
Parasitic Separation	D_s	4.5	mm
Substrate Height	H_1	0.25	mm
Substrate Heights	$H_2 = H_3$	0.5	mm
Relative Dielectric Permittivities	$\epsilon_1 = \epsilon_2 = \epsilon_3$	3	

3.2 Antenna System Architecture

The architecture of the antenna system designed for this research consists of three printed circuit board (PCB) layers, namely feed, antenna, and parasitic layers. In addition to the antenna geometry, the antenna system contains components necessary to the steering function and operation, including the varactor voltage supplying microstrip lines in the bottom surface of the feed layer, the SMA End Launch RF connector, vias, and jumper pins header for the varactor supply voltage. Figure 8 shows a rendered 3D model of the RA board, where Figure 8a shows the top view and Figure 8b shows the bottom view.

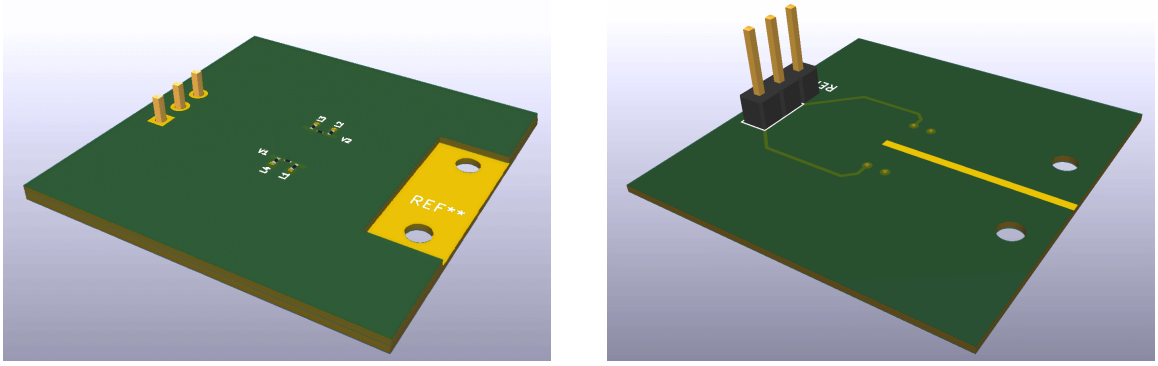

(a) Top view (b) Bottom view

Fig. 8: 3D views of varactor based MRA board

3.2.1 Feeding Layer

As shown in Figure 6, the feed layer has a driven microstrip line on the bottom and ground plane on the top. The ground plane has an aperture slot in its center. The feeding microstrip line passes directly under the aperture. The portion of the microstrip that extends beyond the point directly under the aperture is called the tuning stub. The width of the microstrip feedline is $W_f = 0.62\,\text{mm}$ resulting in a characteristic impedance of 50 ohms at 28 GHz. Along with the RF feed line, the feeding layer also has three DC varactor biasing voltage lines that connect the jumper header to plated vias. As shown in Figure 8, the plated vias connect to the parasitic pixel elements through RF chokes. The DC varactor

biasing voltage lines were placed on the bottom of the Feeding Layer because the ground plane separates them from the radiating elements and reduces their impact on the radiated antenna pattern.

3.2.2 Antenna Layer

Above the feed layer is the antenna layer. The antenna layer has a square patch antenna on its top surface, above the aperture in the ground plane. A patch antenna was chosen as the radiating element due to its low profile, ease of manufacture, and relatively low cost. The patch antenna feeding scheme was chosen to be aperture coupling to reduce the effects of the transmission line on the radiated beam by separating them with a ground plane. Aperture coupled patch antennas also offer broader bandwidth and a high degree of freedom in impedance tuning. The microstrip patch element is square and its width W_p and length L_p are optimized to be 2.284 mm to be resonant at 28 GHz. The feeding scheme for the antenna element is by aperture coupling.

3.2.3 Parasitics Layer

Above the antenna layer is the parasitic layer. The parasitic layer has four microstrip elements on its top surface called parasitic pixels. The parasitic pixels are microstrip segments that run in the same direction as the feeding microstrip line in the feed layer. Two parasitic pixels on a given side form an interconnected pair that make up a parasitic strip or parasitic element. The parasitic elements run parallel and in the same direction as the feeding microstrip line in the feed layer and are normal to the azimuth plane. The parasitic pixel elements in a parasitic strip are separated by a 0.4 mm gap. A varactor diode across the gap connects the parasitic pixel elements. By changing their junction capacitance, these varactor diodes effectively change the parasitic pixels' electric length, resulting in a change in phase in the current induced in the pixel by the coupled patch antenna. This change in the parasitic element's electric lengths causes the radiated beam to steer in the azimuth plane.

The reconfigurable parasitic pixel layer is placed in the near field of the radiating patch

antenna element, thus changing the reactive loading of the antenna element. Depending on their effective electric lengths, these parasitic pixels couple with the driven element and act as reflectors or directors. This effect created by the parasitic pixel elements to reflect or direct the radiated beam of the antenna causes beam steering for the overall radiated beam. The continuously changeable varactor capacitance allows the parasitic element's effective lengths to be changed continuously, thus creating the effect of a continuously steerable radiated beam, which is one of the major novelties of this research.

3.3 Optimization Procedure

The initial simulations were performed on the ideal case, where the varactors were omitted, and the parasitic pixels had their lengths parameterized and physically lengthened or shortened to achieve steering. The motivation of this initial simulation phase was to achieve steering early in the design for a baseline to work from and allow for flexibility in secondary parts of the RA such as the feeding technique or the PCB material as these parameters are simpler to change early on in the design process.

A fixed size for the optimized parasitics was then set, and the varactors were introduced. At this stage, the viability was explored as different techniques of realizing the effects of physically lengthening parasitic pixels through changing the electrical length by changing the capacitance of the varactor. A crucial part of this stage was how the varactor diode version of the design differs from the ideal case and adjusting accordingly. Figure 9 shows five beams of the optimized RA demonstrating the continuous beam steering.

After adjusting the design and achieving steering in the ideal varactor case, the model was altered to a physically realizable version, accounting for how the antenna would be fabricated and including the varactor biasing networks.

3.4 Design Methods and Project Objectives

This project had three stages. 1) The first stage was the full-wave EM design and simulation of the RA, 2) The second stage was the fabrication of the designed RA, 3) The third stage was the test and characterization of the fabricated RA.

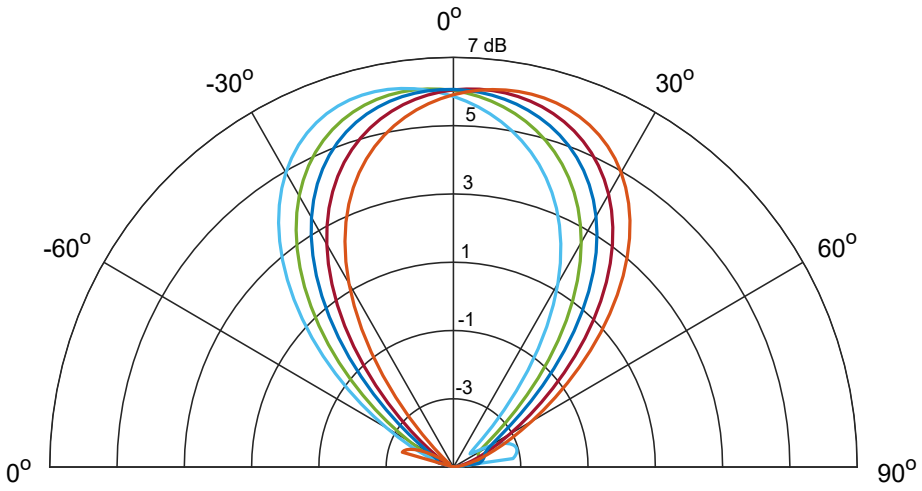

Fig. 9: Beam steering achived in full-wave analysis from optimized RA

This research accomplished three main objectives. The first objective is to design and simulate with full-wave EM analysis of an RA with continuous beam steering capabilities using varactor diodes. The second and third objectives are the fabrication and characterization of the designed antenna. The success of this research is judged by the level of agreement between simulated and measured impedance and radiation pattern results.

CHAPTER 4

MODELS

In this chapter, the component models used in the design and simulation of the RA are presented and discussed. Special treatment is given to the model of the varactor diode due to its central role in this research. Following the discussion on the varactor diode model is a discussion of the DC biasing circuitry and how each component is modeled.

4.1 Varactor Model

The varactor diode is the main component used to accomplish the beam steering in the designed RA system. The varactor, or varicap, is a diode designed to operate in reverse bias. Reverse bias is when the voltage on the cathode, or N-side, is positive with respect to the anode or P-side. Reverse bias causes the charge carriers to diffuse away from the P-N boundary, creating a region of insulation called the depletion layer. This action creates a junction capacitance in the diode, where positive and negative charge carriers act as parallel plates. The depletion layer thickness increases as the reverse bias voltage increases, thus changing the effective capacitor plate gap, which decreases the junction capacitance. All diodes produce a junction capacitance when in reverse bias, but varactor diodes are designed specifically with this effect in mind.

The behavior of the varactor diode is modeled with an RLC network as shown in Figure 10. A variety of lumped element models for varactors exist, and the choice made by the designer of which to use depends on what behaviors are important and how accurate the model needs to be. For this work's design, a series RLC network was used. Each part of the model can be accounted for by considering the physical parts of the varactor diode component. The two pin or pad connectors will have some resistance, along with some inductance. The connectors occur before and after the internal semiconductor part of the varactor. This makes the resistance and inductance in series with the junction capacitance.

Because this series resistance and inductance are not a part of the desired capacitor behavior, they are considered parasitic. There is also a parasitic capacitance; however, its effect is negligible since the capacitance ratio is more important than the capacitance value. The capacitance ratio C_r is the ratio of the largest junction capacitance that the varactor can provide to the smallest junction capacitance that the varactor can provide, $C_r = \frac{\max[C_j(V)]}{\min[C_j(V)]}$. The capacitance of varactor diodes is generally small, on the order of picofarads to hundreds of picofarads.

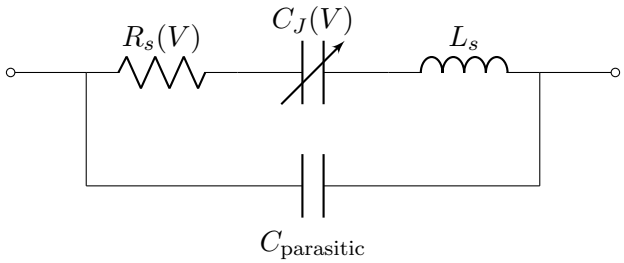

Fig. 10: Schematic of equivalent varactor circuit model

In Figure 10, $R_s(V)$ is the varactor's series parasitic resistance and is a function of applied reverse bias voltage. $C_J(V)$ is the varactor's junction capacitance and is a function of applied reverse bias voltage. L_s is the varactor's series parasitic inductance. And $C_{\text{parasitic}}$ is the varactor's intrinsic parasitic capacitance.

The varactor diode used in the fabricated RA system has a defined relationship between the junction capacitance and the applied reverse bias voltage. Figure 11 shows a plot of this relationship between the junction capacitance C_J and reverse bias voltage V. Along with the junction capacitance, the series resistance of the varactor diode changed depending on the applied reverse bias voltage. Figure 12 shows a plot of this relationship between series resistance R_s and reverse bias voltage V.

Varactor diodes block DC current because they operate in reverse bias. The DC power consumed by the varactor diodes is therefore small compared to PIN diode RF switches, which operate in forward bias.

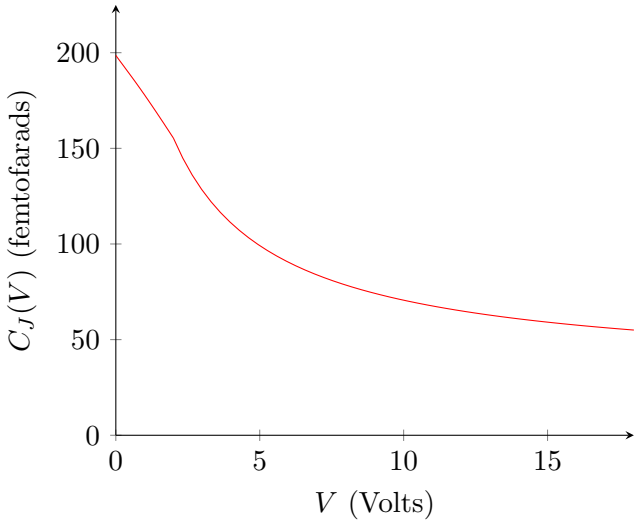

Fig. 11: Varactor junction capacitance vs applied reverse bias voltage

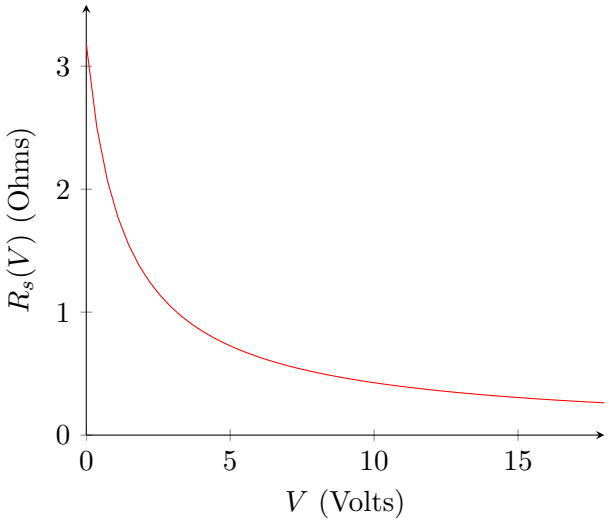

Fig. 12: Varactor series resistance vs applied reverse bias voltage

4.2 Biasing Circuitry Model

The varactor diodes operate in reverse bias. A positive voltage is applied to the cathode of the varactor, and the anode is grounded. The voltage supply is connected to the parasitic pixels through RF Chokes. DC feeding microstrip lines are placed on the feeding layer because the ground plane separates them from the radiating elements. The DC feeding microstrip lines connect to the RF Chokes through plated vias. The RF Chokes prevent the RF signal from going back into the DC power supply.

A photo of the top of the fabricated RA showing the parasitic pixels and the biasing circuit components is shown in Figure 13. In Figure 13, the black rectangles are the surface-mounted components, the two vertical components with a dot at the top are the varactors, and the four horizontal components are the RF Chokes. A lumped model of the DC biasing scheme of the varactor diode is shown in Figure 14.

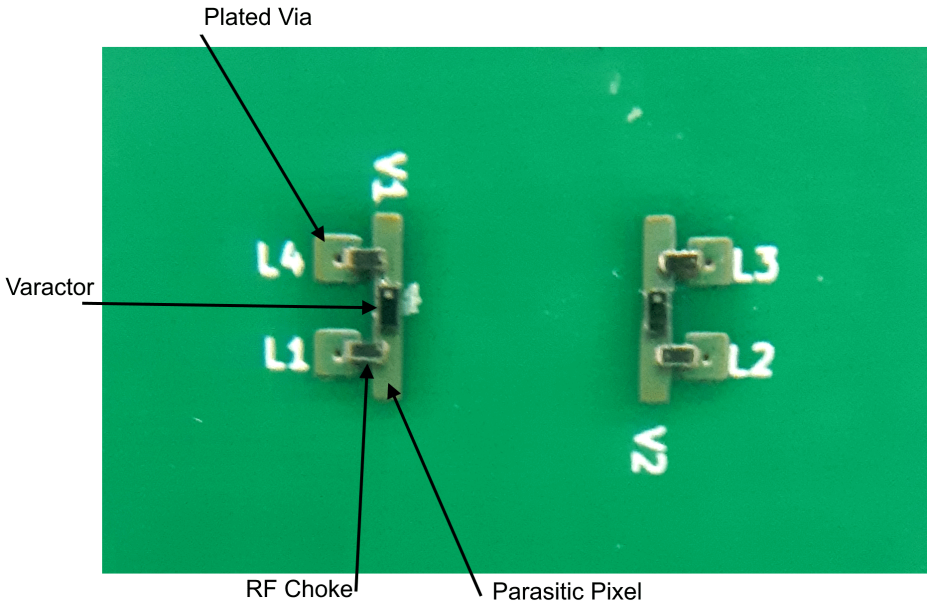

Fig. 13: Parasitic Elements with Varactor Diodes and Chokes

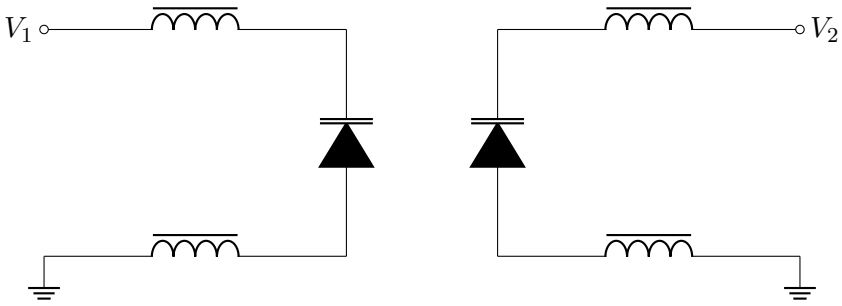

Fig. 14: Biasing circuit schematic diagram showing two varactor diodes along with four RF chokes

CHAPTER 5

WORKING MECHANISM FOR CONTINUOUS BEAM STEERING

This chapter explains and presents an approach for modeling the working mechanism behind how the RA accomplishes beam steering. The approach is to analyze the RA based on the working mechanism of a microstrip Yagi-Uda antenna where an analytical solution is derived. The results from the Yagi-Uda approach are compared against the full-wave analysis results to assess how well it models the RA.

5.1 Yagi Uda Model

The working mechanism behind the beam steering capabilities of the RA designed for this thesis is explained by the Yagi-Uda antenna principle, where the driven antenna element is coupled with parasitic elements that act as directors or reflectors. Figure 15 shows a simple Yagi-Uda antenna using dipole elements; the left element acts as a reflector, the right element acts as a director, and the center element is the driven element. In the RA designed for this thesis, the driven patch antenna is mutually coupled with two reconfigurable pixel-based parasitic strips. The parasitic elements each act as directors or reflectors, depending on their respective electric lengths. The beam will tend to tilt toward the pixel acting as a director, and the beam will tend to tilt away from the pixel acting as a reflector. These two combined effects create the beam steering.

As shown in Figure 17, the parasitic strips are placed above the driven element with vertical distance between the antenna layer and parasitic layer, being 0.08λ at 28 GHz with the relative dielectric permittivity $\epsilon_r = 3$. Since the patch antenna primarily radiates in its broadside direction, this configuration increases the coupling with the parasitic elements. In the case of a traditional dipole Yagi-Uda antenna, as seen in Figure 17, the parasitic element with an electric length longer than the driven element acts as a reflector, and the parasitic element with an electric length shorter than the driven element acts as a director.

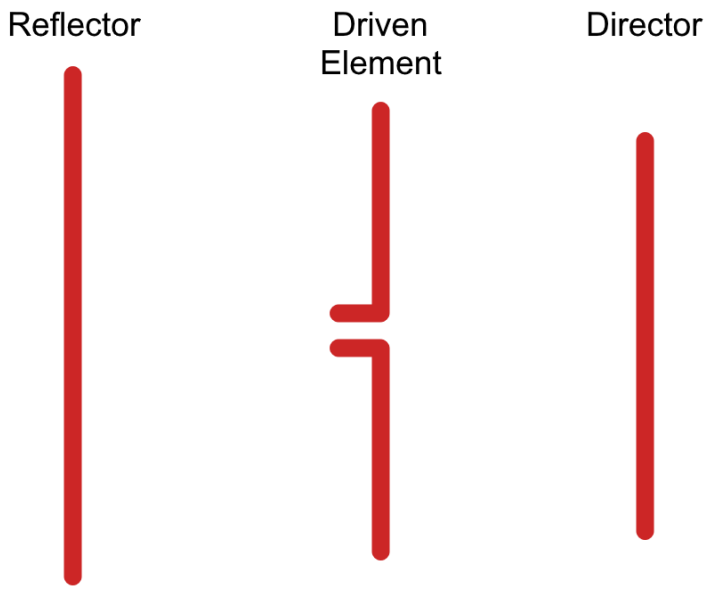

Fig. 15: Basic Yagi-Uda diagram using dipole elements

The behavior of a parasitic element acting as a director or reflector is due to the difference in phase of the induced surface current densities on the parasitic and driven elements.

The varactor diodes capacitively load the parasitic pixels and effectively change the parasitic pixel's electric lengths proportional to the varactor diode's junction capacitance. Because the varactor capacitances are continuously changeable, the electric lengths are continuous, which means that the parasitic pixels can continuously change from a reflector to a director, allowing the beam to be steered continuously.

5.1.1 Derivation of Analytical Model

The field pattern, $\mathrm{F}_a(\theta)$, of the RA system can be modeled based on pattern multiplication principle with the expression given in Equation 5.1 where $\mathrm{EF}(\theta)$ is the element factor and $\mathrm{AF}(\theta)$ is the array factor.

$$\mathrm{F}_a(\theta) = \mathrm{EF}(\theta)\mathrm{AF}(\theta) \tag{5.1}$$

In this model, the parasitic elements are treated like radiating patch antenna elements phase shifting. The RA system is therefore modeled as a three-patch antenna array. Figure

16 shows the elements of the RA in space and the coordinate system in the Yagi-Uda model.

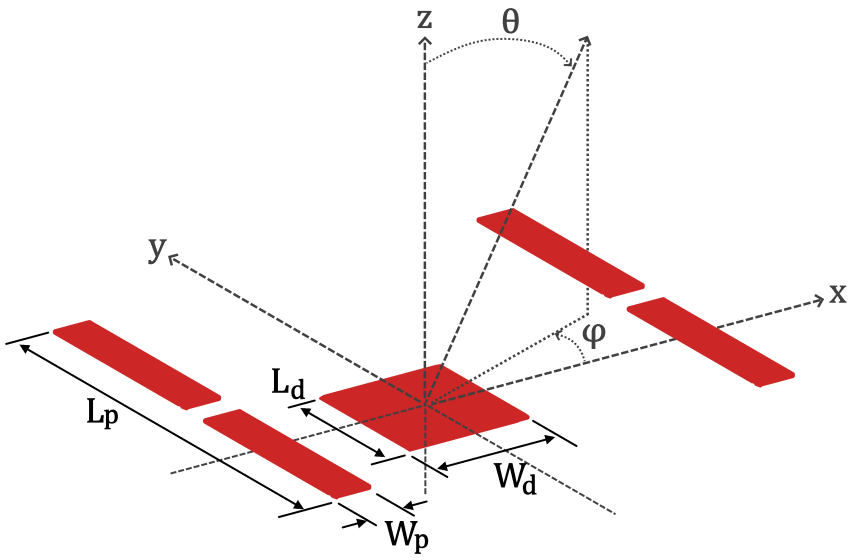

Fig. 16: RA structure consisting of the parasitic elements and driven patch element in space with θ and ϕ direction vectors shown

Figure 17 shows the placement of the antenna elements 1, 2, and 3 in the array model, where element 1 is the driven patch antenna element, and elements 2 and 3 are the parasitic elements.The elements in Figure 17 are represented as a points in the $\phi = 0$ plane, and are expressed as position vectors $\mathbf{p}_1$, $\mathbf{p}_2$, and $\mathbf{p}_3$.

The array factor of the antenna array given in Figure 17 can be found as given in Equation 5.2.

$$\mathrm{AF}(\theta) = w_1 e^{-jk_0\hat{\mathbf{r}}\cdot\mathbf{p}_1} + w_2 e^{-jk_0\hat{\mathbf{r}}\cdot\mathbf{p}_2} + w_3 e^{-jk_0\hat{\mathbf{r}}\cdot\mathbf{p}_3} \tag{5.2}$$

In Equation 5.2, $\mathbf{p}_1$ is the position of the driven patch, and $\mathbf{p}_2$ and $\mathbf{p}_3$ are the positions of the parasitic elements. k_0 is the phase constant for free space at 28 GHz, and w_1, w_2, and w_3 are weights for each element. The driven patch antenna is placed on the origin, which makes the product of $\hat{\mathbf{r}} \cdot \mathbf{p}_1 = 0$. The two parasitic elements have position vectors of $\mathbf{p}_2 = -d\hat{\mathbf{x}} + h\hat{\mathbf{z}}$ and $\mathbf{p}_2 = d\hat{\mathbf{x}} + h\hat{\mathbf{z}}$, where $d = \frac{D_s}{2} = 2.25\,\mathrm{mm}$ and $h = 0.5\,\mathrm{mm}$. The

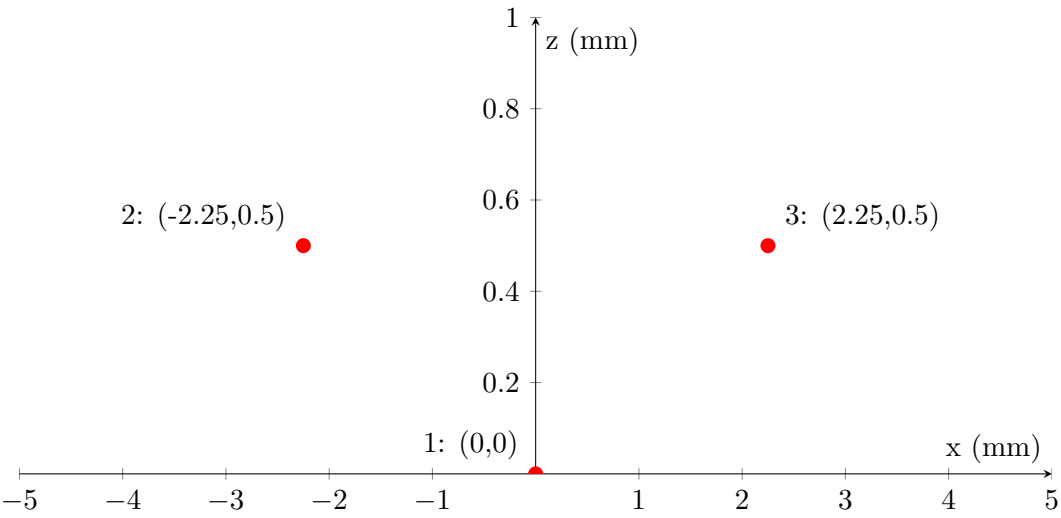

Fig. 17: Placement of antenna elements in phased array model of RA system, 1 corresponds to the driven patch element, 2 and 3 correspond to the parasitic elements

opservation point direction unit vector is $\hat{\mathbf{r}} = (\sin(\theta)\cos(\phi)\hat{\mathbf{x}} + \sin(\theta)\sin(\phi)\hat{\mathbf{y}} + \cos(\theta)\hat{\mathbf{z}})$. The steering occurs only in the x-z plane, therefore only positions where $\phi = 0$ are necessary for this model. Plugging in these values into Equation 5.2 gives Equations 5.3 and eqn:af2b.

$$\mathrm{AF}(\theta) = w_1 + w_2 e^{-jk_0\hat{\mathbf{r}}\cdot\mathbf{p}_2} + w_3 e^{-jk_0\hat{\mathbf{r}}\cdot\mathbf{p}_3} \tag{5.3}$$

$$\mathrm{AF}(\theta) = w_1 + w_2 e^{-jk_0(-d)\sin\theta + h\cos\theta} + w_3 e^{-jk_0 d\sin\theta + h\cos\theta} \tag{5.4}$$

The element factors are not the same for each element, therefore each element term in the array factor is multiplied by its corresponding element factor. Equation 5.5 gives the element factor, $F_1(\theta)$, of the driven patch antenna element, and Equation 5.6 gives the element factors, $F_2(\theta)$ and $F_3(\theta)$, of the parasitic elements. In Equation 5.5, $W_d = 2.284\,\mathrm{mm}$ is the width of the driven patch antenna element and $L_d = 2.284\,\mathrm{mm}$ is the length of the driven patch antenna element. In equation 5.6, $W_p = 0.5\,\mathrm{mm}$ is the width of each parasitic pixel element and $L_p = 3.5\,\mathrm{mm}$ is the length of of each parasitic pixel element.

$$F_1(\theta) = \frac{\sin\left[\frac{k_0 W_d}{2}\sin\theta\right]}{\frac{k_0 W_d}{2}\sin\theta}\cos\left(\frac{k_0 L_d}{2}\sin\theta\right)\cos\theta \tag{5.5}$$

$$F_2(\theta) = F_3(\theta) = \frac{\sin\left[\frac{k_0 W_p}{2}\sin\theta\right]}{\frac{k_0 W_p}{2}\sin\theta}\cos\left(\frac{k_0 L_p}{2}\sin\theta\right)\cos\theta \tag{5.6}$$

An expression for the total far-field radiation pattern of the RA based on a Yagi-Uda antenna approach is given in Equation 5.7 is found by combining Equations 5.4 and Equations 5.5 and 5.6

$$F_a(\theta) = F_1(\theta) + \frac{I_2}{I_1}F_2(\theta)e^{jk_0 d\sin(\theta)\left[1-\frac{h\cot(\theta)}{d}\right]} + \frac{I_3}{I_1}F_3(\theta)e^{-jk_0 d\sin(\theta)\left[1+\frac{h\cot(\theta)}{d}\right]}. \tag{5.7}$$

In Equation 5.7, I_1, I_2, and I_3 are the weighting complex currents in element 1, 2, 3 respectively. The lateral distance between the parasitic elements are $d = \frac{D_s}{2} = 2.25\,\text{mm}$ and the vertical separation between the patch element and the parasitic layer is $h = 0.5\,\text{mm}$. The field pattern of the elements in isolation can be approximated using the field pattern of a patch antenna $F(\theta)$. The field patterns are given in equation 5.5 and equation 5.6

The complex currents $I_1, I_2,$ and I_3 are calculated by integrating the magnetic fields $H_1, H_2,$ and H_3 along the closed curves $C_1, C_2,$ and C_3 enclosed around the surface current in each element, respectively.

Two cases were evaluated and compared with the full-wave analysis result. Given the case where $V_1 = 0.4\,\text{V}$ and $V_2 = 18\,\text{V}$, the complex currents were calculated to be

$$\frac{I_2}{I_1} = 0.8\exp(-j2.5)$$
$$\frac{I_3}{I_1} = 0.1\exp(-j3.8).$$

These complex currents are used in Equation 5.7 to calculate the Yagi-Uda Patch Antenna field pattern, which is compared against the full-wave analysis result in Figure 18. This is

a steered beam case.

Given another case where $V_1 = 18\,\mathrm{V}$ and $V_2 = 18\,\mathrm{V}$, the complex currents were calculated to be

$$\frac{I_2}{I_1} = 0.4\exp(-j2)$$
$$\frac{I_3}{I_1} = 0.4\exp(-j2).$$

These complex currents used in Equation 5.7 result in the normailized field patterns shown in Figure 19.

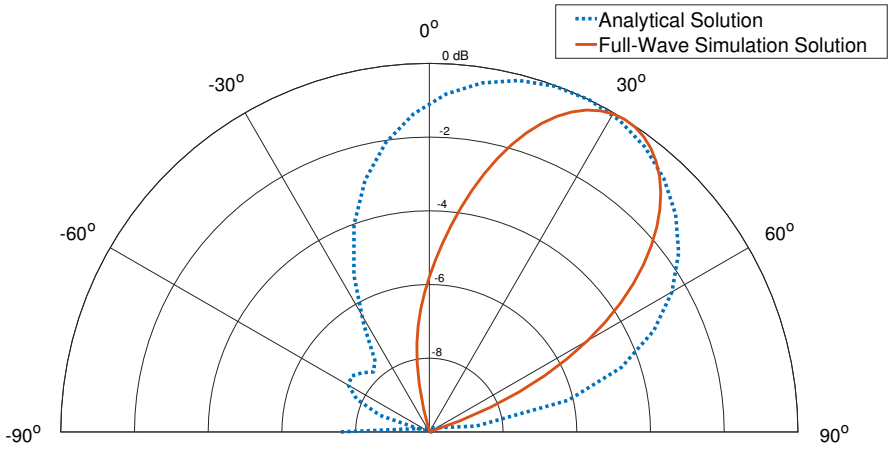

Fig. 18: Analytical field pattern solution compared with simulated full wave analysis for the $V_1 = 0.4\,\mathrm{V}$ and $V_2 = 18\,\mathrm{V}$ case

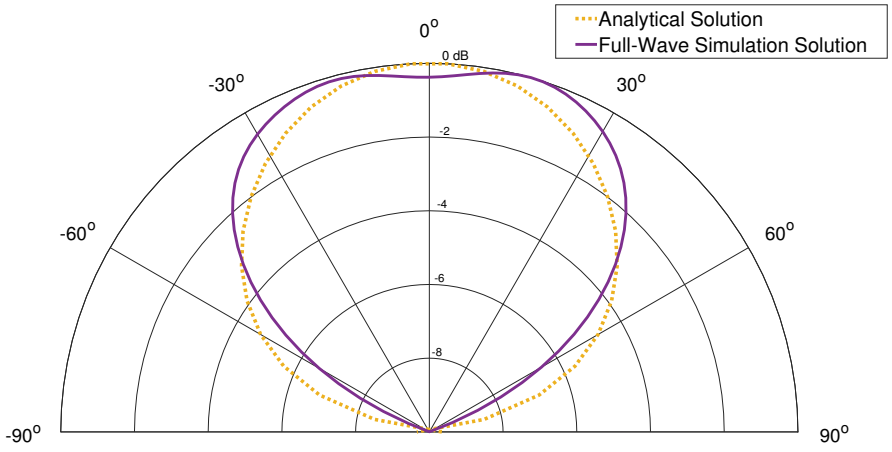

Fig. 19: Analytical field pattern solution compared with simulated full wave analysis for the $V_1 = 18\,\mathrm{V}$ and $V_2 = 18\,\mathrm{V}$ case

CHAPTER 6

FABRICATION

A working prototype of the RA was fabricated by a 3rd party printed circuit board (PCB) manufacturer. The fabricated RA was tested and used to assess the accuracy of the analytical models and simulation results. Before fabrication, the PCB stack-up and the PCB materials, prepregs, and electronic parts were prepared and sent to the PCB manufacturer. The antenna design was recreated in a PCB design program, exported in the gerber file format, and sent to the PCB manufacturer. The fabricated antenna was characterized in an anechoic chamber, and the measured results were compared with those obtained from the simulated full-wave analysis. The continuous steering was tested by measuring small changes to the pattern resulting from small changes to the varactor bias voltages.

This chapter outlines the design decisions necessary for fabrication and the process behind manufacturing the RA prototype. This chapter also discusses the finished RA prototype and what changes could result in a better product.

6.1 Fabrication Decisions

The PCB material chosen was MT77 due to its desirable electrical properties ($\epsilon_r = 3$, $\tan\delta = 0.0013$) and its physical properties such as its strength and rigidity. These properties enable a robust and high yield vertical via formation process in a multilayered PCB stack-up.

A necessary addition to the RA design for fabrication was the cavity from the parasitic layer down to the ground layer. This cavity is for the end-launch RF connector, requires the feed line and the ground plane exposed. Since the ground plane is an internal layer, the layers above the ground layer and the size and shape housing the RF connector needed to be milled away. Figure 20 shows the cavity and its dimensions.

Table 6.1 lists the makes and models for all the components used in the biasing network.

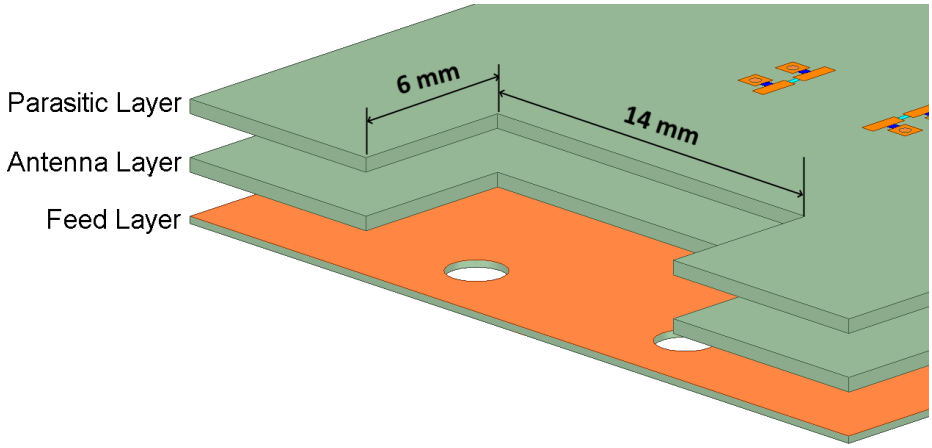

Fig. 20: Exploded 3D view of antenna board showing the milled cavity for housing the RF end launch connector

Table 6.1: Bill of Materials

Component Model	Manufacturer	Device	Value
MAVR-011020-1411	MACOM	Varactor Diode	0.081 pF at 4 V
L0201	AVX	RF Choke Inductor	0.82 nH
87891-0306	Molex	2.54 mm Jumper Header	
1492-04Z5	Southwest Microwave	2.4 SMA Jack (female)	

6.2 Fabricated Antenna

Figure 21 shows photographs of the top and bottom of one of the fabricated prototype RA boards fabricated by a PCB manufacturer. The top of the RA board is the radiating side of the antenna. The bottom of the RA board is where the signal is fed to the antenna. In addition to the antenna board, Figure 21 shows the end launch RF SMA connector, showing the relative size of the connector to the RA board. The large metal end launch connector negatively impacts the overall radiated pattern and antenna performance. A redesign replacing the large side-fed connector with a smaller connector behind the ground plane would improve the RA system's current iteration by reducing the connector's negative impact.

6.3 Non-functional Components

Non-functional Components are parts of the overall system that do not contribute to

the radiation, beam steering, or any working mechanism of the RA but are necessary to facilitate the measurement. The non-functional components outlined in this section were primarily used to facilitate the measurement of the RA.

6.3.1 Anechoic Chamber

The anechoic chamber used for measuring the RA was a millibox millimeter-wave anechoic chamber. The antenna was mounted on a gimbal that can rotate around the horizontal and vertical axis, allowing for three-dimensional measurements. The receiving antenna used was a horn antenna mounted in the anechoic chamber in the far-field of the device under test (DUT) RA.

6.3.2 Mount

A mounting platform for the RA to fit into the anechoic chamber was designed and 3D printed. The mounting platform was bolted onto the gimbal in the anechoic chamber and was used to hold the RA in place and allow the gimbal to rotate the RA for measurement. The mounting platform was 3D printed using acrylonitrile butadiene styrene (ABS) plastic.

6.3.3 Power Supply

A Rigol DP832A DC digital three-channel power supply was used to provide the two varactor DC bias voltages. Two power supply channels were used, one for each varactor bias

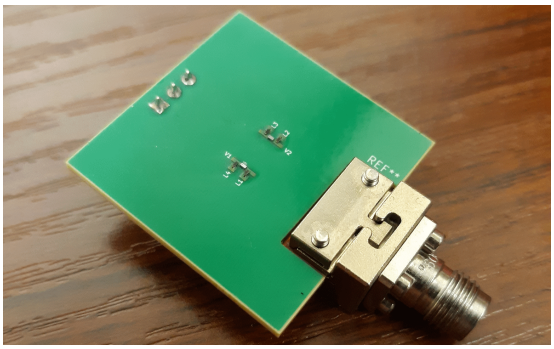

(a) Top of RA prototype

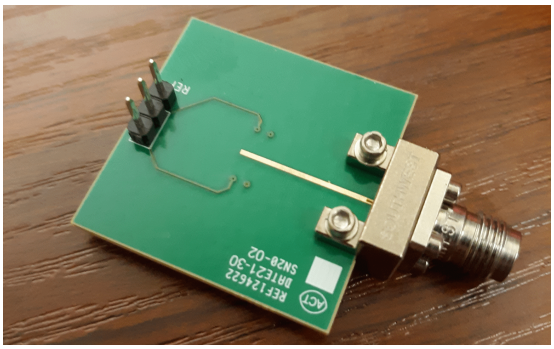

(b) Bottom of RA prototype

Fig. 21: Photos of RA board

voltage V_1 and V_2. The power supply is connected to the RA prototype board through cables attached to the jumper header pins. The power supply cables were positioned behind the RA prototype board to reduce their effects on the radiation pattern. The total DC power consumed was calculated by adding the power consumed by the two channels. The DC power consumed by the RF switching circuitry was determined by the displayed current and voltage on the power supply.

CHAPTER 7

RESULTS

This chapter presents the fabricated antenna measurements and compares the results with their respective simulation results. Key metrics are used to assess the antenna, including the reflection coefficient, the gain, the steering, and the power consumption by the switching circuitry.

The measurements were done in a millimeter-wave anechoic chamber, with a VNA as the measurement instrument. The varactor voltages were supplied using a digital power supply. The reflection coefficient was measured, with the desired center frequency below $-10\,\mathrm{dB}$, one criterion used to determine sufficient power radiation. The voltage standing wave ratio VSWR was determined to be below 2, another criterion for determining if sufficient power is radiating.

7.1 Characterization And Testing Of The Fabricated Antenna

The continuous steering capabilities of the RA are demonstrated by characterizing the antenna in an anechoic chamber and comparing these measurements to full-wave EM analysis. To this end, the varactor reverse bias voltages are applied with various voltage values corresponding to simulated steering modes; these measurements will be compared with the simulations corresponding to each mode. The following are critical aspects of the measurements to be compared with simulation:

- Main lobe direction
- Realized Gain
- Half-power beam width
- Reflection coefficient

This section presents the measurements that were carried out to characterize the fabricated RA prototype. First, the non-functional parts of the measurement, including the anechoic chamber, the 3D printed antenna mounting stand, and the power supply, are discussed. Second, this chapter also outlines the essential requirements used to show that the fabricated RA sufficiently matched the full-wave analysis model. These requirements include the reflection coefficient or S11 parameter. The tests outlined in this chapter show that the fabricated antenna and full-wave analysis model sufficiently agree, which gives confidence in the measurements used to assess the beam steering.

7.1.1 Measurements

The reflection coefficient for the RA was measured using a MS4647B Anritsu Vector Network Analyzer with two-port Short-Open-Load-Through (SOLT) calibration. The reflection coefficient was measured with the bias voltages set to $V_1 = V_2 = 18\,\mathrm{V}$. Figure 22 shows the measured reflection coefficient of the fabricated prototype RA compared with the full-wave analysis simulation reflection coefficient result. The measured reflection coefficient agrees reasonably well with simulation.

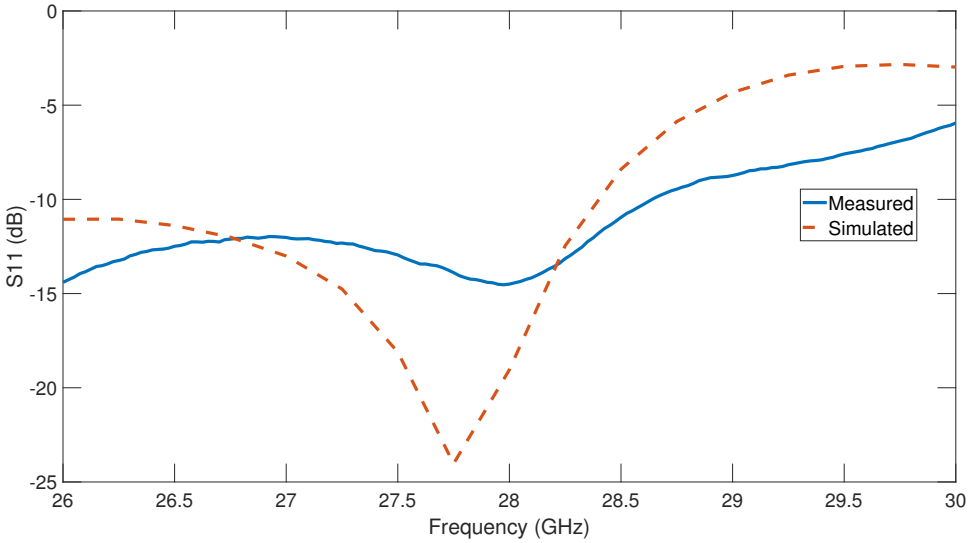

Fig. 22: Reflection coefficent of fabricated RA compared with reflection coefficent of full-wave analysis simulation, both for the case of $V_1 = 0.4\,\mathrm{V}$, $V_2 = 18\,\mathrm{V}$

7.1.2 Reflection Coefficient Change with Varactor Bias Voltage

The reflection coefficient for the RA changed depending on the supplied DC varactor bias voltages. This behavior is expected based on the simulation results and shows that the radiating patch antenna element is coupling with the parasitic elements because the coupled parasitic elements change the reactive loading of the patch antenna. During the measurement, the varactor voltages were configured in three cases. Case 1 was where $V_1 = V_2 = 0\,\mathrm{V}$. Case 2 was where $V_1 = 0.4\,\mathrm{V}$, $V_2 = 18\,\mathrm{V}$. Case 3 was where $V_1 = V_2 = 18\,\mathrm{V}$. Figure 23 shows the reflection coefficient measurement result of the fabricated RA prototype board for the three cases.

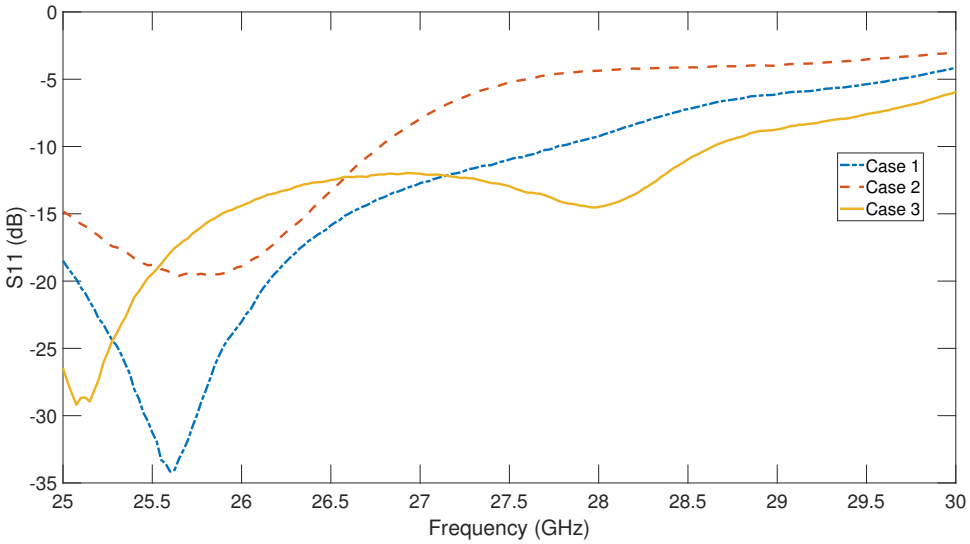

Fig. 23: Reflection coefficent of fabricated RA for three cases of applied bias voltages

7.1.3 DC Power Consumption

The peak DC current used by the RF switching circuitry is $\approx 1\,\mathrm{mA}$ at $18\,\mathrm{V}$. The peak DC power consumed by the steering circuitry during operation is therefore calculated as $2(18\,\mathrm{V} \cdot 1\,\mathrm{mA}) = 36\,\mathrm{mW}$. The measured reverse bias current through the varactors stayed relatively constant for all applied reverse bias voltages, making the DC power consumed by a given varactor proportional to the applied reverse bias voltage. The total DC power

consumed, P_t, was measured at various applied reverse bias voltages as seen in Table 7.1.

Table 7.1: DC power consumed for various varactor reverse bias voltages

V_1 (V)	V_2 (V)	P_t (mW)
0.4	0.4	0.8
1	1	2
2	2	4
3	3	6
4	4	8
5	5	10
6	6	12
7	7	14
8	8	16
9	9	18
10	10	20
11	11	22
12	12	24
13	13	26
14	14	28
15	15	30
16	16	32
17	17	34
18	18	36

7.2 Steering

Various voltage values were set for the varactor bias voltages V_1 and V_2 to test the steering capabilities of the fabricated RA. Then for each varactor vias voltage pair, the antenna was rotated through the plane of steering in steps of 5° with a measurement sample taken at every step. A full-wave analysis antenna model was simulated with a range of voltages for V_1 and V_2, between 0 and 18 Volts each. The measured data points and the full-wave analysis simulation results were plotted with the same varactor bias voltages. Table 7.2 gives the measurements of half-power beam width, main lobe direction, and realized gain of the fabricated RA. Table 7.3 gives the results for many voltage configurations. The voltage configurations in Table 7.3 were chosen based on simulation results showing a promising beam. Figures 24, 25, 26, 27, and 28 show the plot of the radiation pattern of

the fabricated antenna and simulated radiation pattern for given varactor bias voltages of five selected beams.

Table 7.2: Measurements of half-power beam width, main lobe direction, and realized gain of the fabricated RA

V_1(V)	V_2(V)	Half-power beam width (Degrees)	Main lobe direction (Degrees)	Realized Gain (dB)
18	18	82	-4	7.4
0.4	18	42	50	7.5
18	0.4	22	-30	8.4
0.4	10	42	50	7.5
10	0.4	16	33	7.25

Table 7.3: Measurements of beam steering of the fabricated RA

V_1(V)	V_2(V)	Peak beam direction (Degrees)	Max Gain (dB)
18	1	-30	6.94
18	0.4	-30	6.85
15	1	-28	6.7
10	0.4	-28	6.66
10	1	-28	6.46
3.5	0.4	-28	4.56
18	2	-26	6.71
18	3	-26	6.56
7	17	-10	7.39
7.6	3	-10	6.34
18	15	-4	7.72
18	18	-4	7.71
15	18	-4	7.68
17	11	-4	7.56
17	7	-4	7.44
11	7	-4	7.4
12.2	4.5	-4	6.85
4.5	12.2	-4	6.44
1	10	34	6.27
2	18	34	5.98
0.4	3.5	34	3.56
1	15	36	6.47
0.4	18	36	6.33
0.4	10	36	6.15
3	7.6	36	5.54
3	18	36	5.45
1	18	38	6.37

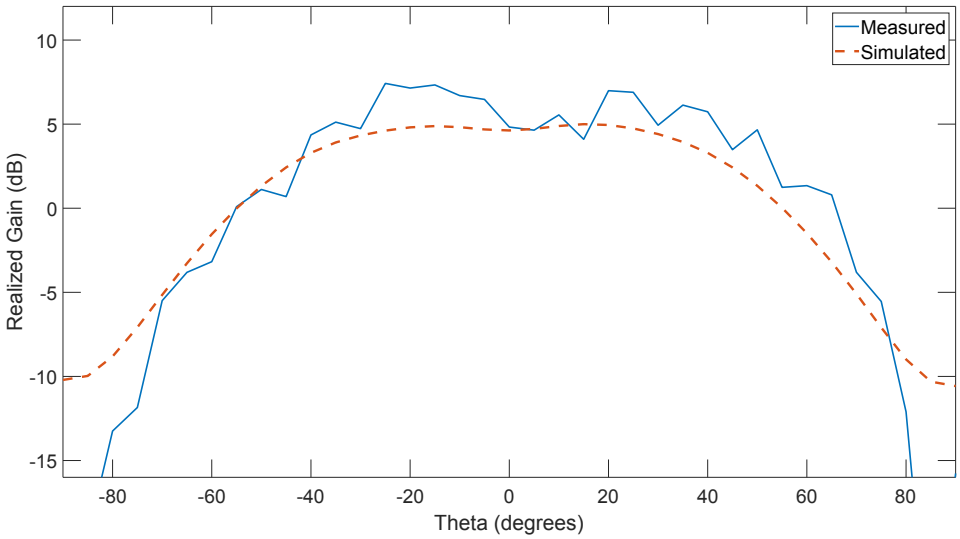

Fig. 24: Measured and simulated RA radiated patterns where $V_1 = 18\,\mathrm{V}$ and $V_1 = 18\,\mathrm{V}$

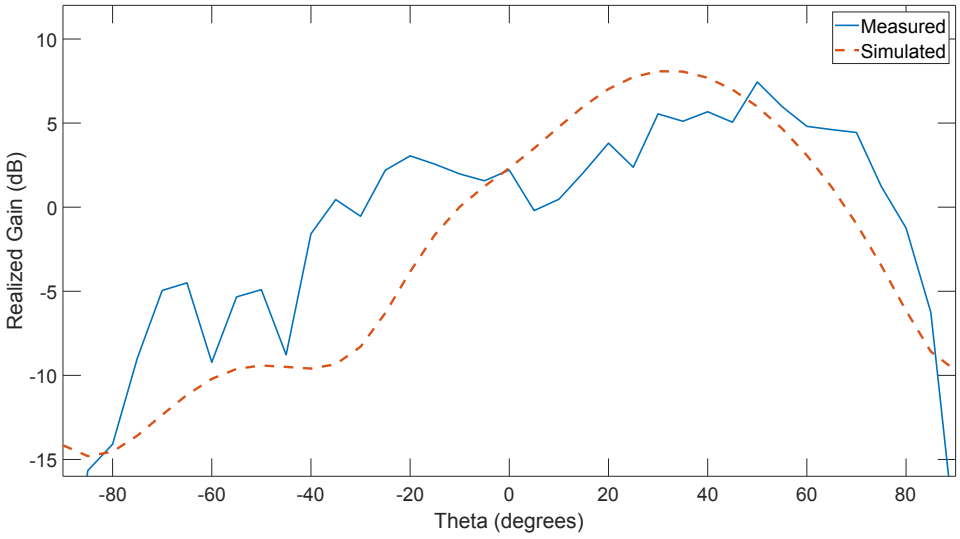

Fig. 25: Measured and simulated RA radiated patterns where $V_1 = 0.04\,\mathrm{V}$ and $V_1 = 18\,\mathrm{V}$

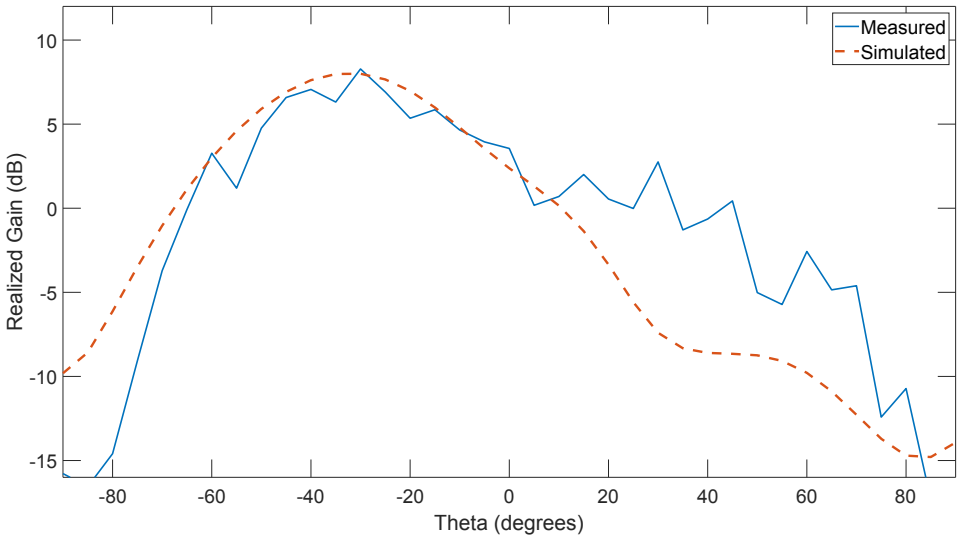

Fig. 26: Measured and simulated RA radiated patterns where $V_1 = 18\,\mathrm{V}$ and $V_1 = 0.04\,\mathrm{V}$

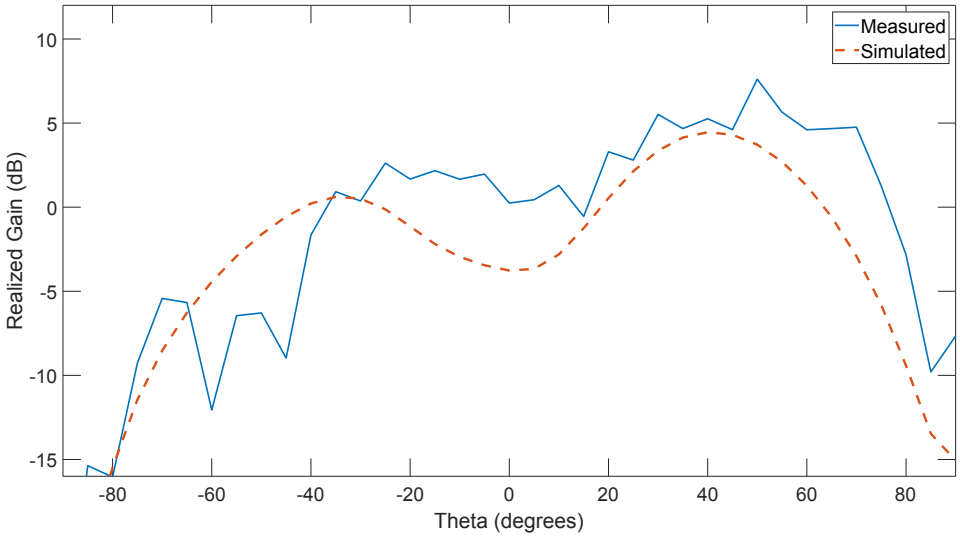

Fig. 27: Measured and simulated RA radiated patterns where $V_1 = 0.04\,\mathrm{V}$ and $V_1 = 10\,\mathrm{V}$

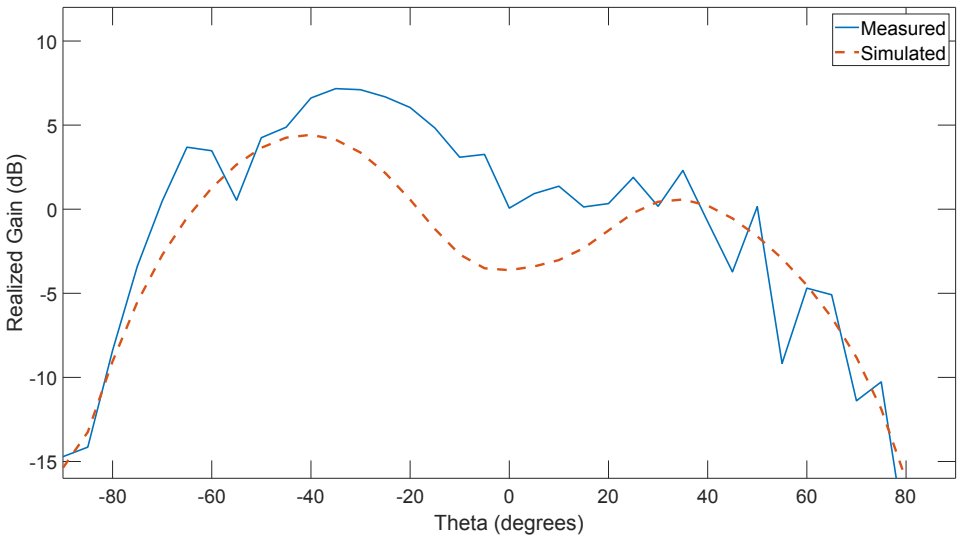

Fig. 28: Measured and simulated RA radiated patterns where $V_1 = 10\,\mathrm{V}$ and $V_1 = 0.04\,\mathrm{V}$

CHAPTER 8

CONCLUSION

To meet the need for the increasing wireless data demands, broader bandwidths are needed. These needs are met by using higher and higher electromagnetic frequencies, which comes with many challenges that must be met. Reconfigurable antennas (RAs) have become a popular area of research. They overcome many drawbacks of traditional legacy antennas. Additionally, they provide the functionality of large antenna systems and arrays with less power consumption and smaller and simpler architectures, and less complexity. This project builds upon the existing RA designs by making the beam steering capability of previous PIN diode solutions continuous through the use of varactor diodes. The use of varactor diodes reduces the amount of power consumption and the complexity of the design by reducing the number of needed components to achieve a large number of steering modes. An RA using varactor diodes was designed, fabricated, and characterized. The results of the characterization and testing showed that the antenna had continuous beam steering with less DC power consumption by the switching circuitry compared with previous PIN diode solutions.

REFERENCES

[1] J. Kalliovaara, T. Jokela, H. Kokkinen, and J. Paavola, "Licensed shared access evolution to provide exclusive and dynamic shared spectrum access for novel 5g use cases," in *Cognitive Radio in 4G/5G Wireless Communication Systems*, S. S. Moghaddam, Ed. Rijeka: IntechOpen, 2018, ch. 3. [Online]. Available: https://doi.org/10.5772/intechopen.79553

[2] J. Costantine, Y. Tawk, and C. G. Christodoulou, *Reconfigurable Antennas*. Singapore: Springer Singapore, 2016, pp. 1737–1772. [Online]. Available: https://doi.org/10.1007/978-981-4560-44-3_61

[3] Z. Li, D. Rodrigo, L. Jofre, and B. A. Cetiner, "A new class of antenna array with a reconfigurable element factor," *IEEE Transactions on Antennas and Propagation*, vol. 61, no. 4, pp. 1947–1955, 2013.

[4] M. A. Towfiq, I. Bahceci, S. Blanch, J. Romeu, L. Jofre, and B. A. Cetiner, "A reconfigurable antenna with beam steering and beamwidth variability for wireless communications," *IEEE Transactions on Antennas and Propagation*, vol. 66, no. 10, pp. 5052–5063, 2018.

[5] D. Rodrigo, J. Romeu, B. Cetiner, and L. Jofre, "Pixel reconfigurable antennas: Towards low-complexity full reconfiguration," 04 2016, pp. 1–5.

[6] W. Delaney, "From vision to reality 50+ years of phased array development," in *2016 IEEE International Symposium on Phased Array Systems and Technology (PAST)*, 2016, pp. 1–8.

[7] D. Berry, R. Malech, and W. Kennedy, "The reflectarray antenna," *IEEE Transactions on Antennas and Propagation*, vol. 11, no. 6, p. 645–651, 1963.

[8] H. Tian, L. Jiang, and T. Itoh, "A compact single-element pattern reconfigurable antenna with wide-angle scanning tuned by a single varactor," *Progress In Electromagnetics Research C*, vol. 92, pp. 137–150, 01 2019.

[9] K. Narayanasamy, G. N. A. Mohammed, K. Savarimuthu, R. Sivasamy, and M. Kanagasabai, "A comprehensive analysis on the state-of-the-art developments in reflectarray, transmitarray, and transmit-reflectarray antennas," *International Journal of RF and Microwave Computer-Aided Engineering*, vol. 30, no. 9, p. e22272, 2020. [Online]. Available: https://onlinelibrary.wiley.com/doi/abs/10.1002/mmce.22272

[10] S. V. Hum and J. Perruisseau-Carrier, "Reconfigurable reflectarrays and array lenses for dynamic antenna beam control: A review," *IEEE Transactions on Antennas and Propagation*, vol. 62, no. 1, pp. 183–198, 2014.

[11] S. Hum, M. Okoniewski, and R. Davies, ""realizing an electronically tunable reflectarray using varactor diode-tuned elements"," *Microwave and Wireless Components Letters, IEEE*, vol. 15, pp. 422 – 424, 07 2005.

[12] M. Riel and J.-J. Laurin, "Design of an electronically beam scanning reflectarray using aperture-coupled elements," *IEEE Transactions on Antennas and Propagation*, vol. 55, no. 5, pp. 1260–1266, 2007.

[13] ——, "Design of a C-band reflectarray element with full phase tuning range using varactor diodes," 08 2005, pp. 622 – 625 vol. 3A.

[14] O. G. Vendik and M. Parnes, "A phase shifter with one tunable component for a reflectarray antenna," *IEEE Antennas and Propagation Magazine*, vol. 50, no. 4, pp. 53–65, 2008.

[15] M. H. Dahri, M. H. Jamaluddin, F. C. Seman, M. I. Abbasi, N. F. Sallehuddin, A. Y. I. Ashyap, and M. R. Kamarudin, "Aspects of efficiency enhancement in reflectarrays with analytical investigation and accurate measurement," *Electronics*, vol. 9, no. 11, p. 1887, 2020.

[16] D. Pozar, S. Targonski, and H. Syrigos, "Design of millimeter wave microstrip reflectarrays," *IEEE Transactions on Antennas and Propagation*, vol. 45, no. 2, p. 287–296, Feb 1997.

[17] S. H. Zainud-Deen, S. M. Gaber, and K. Awadalla, "Transmitarray using perforated dielectric material for wideband applications," *Progress in Electromagnetics Research M*, vol. 24, pp. 1–13, 2012.

[18] C. Liaskos, A. Tsioliaridou, A. Pitsillides, I. F. Akyildiz, N. V. Kantartzis, A. X. Lalas, X. Dimitropoulos, S. Ioannidis, M. Kafesaki, and C. Soukoulis, "Design and development of software defined metamaterials for nanonetworks," *IEEE Circuits and Systems Magazine*, vol. 15, no. 4, pp. 12–25, 2015.

[19] C. Liaskos, A. Tsioliaridou, A. Pitsillides, S. Ioannidis, and I. Akyildiz, "Using any surface to realize a new paradigm for wireless communications," *Communications of the ACM*, vol. 61, no. 11, p. 30–33, 2018.

[20] A. M. Khalat, "Multifunctional reconfigurable antennas and arrays operating at 60 ghz band," Ph.D. dissertation, Utah State University, Logan, Utah, 2017.

[21] M. A. Hossain, I. Bahceci, and B. A. Cetiner, "Parasitic layer-based radiation pattern reconfigurable antenna for 5g communications," *IEEE Transactions on Antennas and Propagation*, vol. 65, no. 12, pp. 6444–6452, 2017.

[22] Z. Li, E. Ahmed, A. M. Eltawil, and B. A. Cetiner, "A beam-steering reconfigurable antenna for wlan applications," *IEEE Transactions on Antennas and Propagation*, vol. 63, no. 1, pp. 24–32, 2015.

[23] D. Rodrigo, B. Cetiner, and L. Jofre, "Frequency, radiation pattern and polarization reconfigurable antenna using a parasitic pixel layer," *Antennas and Propagation, IEEE Transactions on*, vol. 62, pp. 3422–3427, 06 2014.

[24] H.-P. Chang, J. Qian, B. Cetiner, F. De Flaviis, M. Bachman, and G. Li, "Design and process considerations for fabricating RF MEMS switches on printed circuit boards," *Journal of Microelectromechanical Systems*, vol. 14, no. 6, pp. 1311–1322, 2005.

[25] L. Xue, C.-Y. Jiang, H.-L. Chang, Y. Yang, W. Qin, and W.-Z. Yuan, "A novel kalman filter for combining outputs of mems gyroscope array," *Measurement*, vol. 45, no. 4, pp. 745–754, 2012. [Online]. Available: https://www.sciencedirect.com/science/article/pii/S0263224111004532

[26] A. Zohur, H. Mopidevi, D. Rodrigo, M. Unlu, L. Jofre, and B. A. Cetiner, "RF MEMS reconfigurable two-band antenna," *IEEE Antennas and Wireless Propagation Letters*, vol. 12, pp. 72–75, 2013.

[27] X. Yuan, Z. Li, D. Rodrigo, H. S. Mopidevi, O. Kaynar, L. Jofre, and B. A. Cetiner, "A parasitic layer-based reconfigurable antenna design by multi-objective optimization," *IEEE Transactions on Antennas and Propagation*, vol. 60, no. 6, pp. 2690–2701, 2012.

[28] S. N. M. Zainarry, "Reconfigurable antennas based on varactor-loaded stubs," Ph.D. dissertation, The University of Adelaide, Adelaide SA 5005, Australia, 2019.

[29] Y. Tazaki, E. Nishiyama, and M. Aikawa, "Beam steering microstrip antenna with varactor diode," in *Proceedings of ISAP2007, Niigata, Japa*, 2007, pp. 712–715.

[30] J. T. Bernhard, "Reconfigurable antennas," *Synthesis Lectures on Antennas*, vol. 2, no. 1, pp. 1–66, 2007.